Stationary states and instabilities of a Möbius fiber resonator

Calum Maitland,[1,2,*] Matteo Conforti,[3] Arnaud Mussot,[3,4] and Fabio Biancalana[1]

[1]*Institute of Photonics and Quantum Sciences, Heriot-Watt University, Edinburgh EH14 4AS, United Kingdom*
[2]*School of Physics and Astronomy, University of Glasgow, Glasgow G12 8QQ, United Kingdom*
[3]*Université Lille, CNRS, UMR 8523-PhLAM-Physique des Lasers Atomes et Molécules, F-59000 Lille, France*
[4]*Institut Universitaire de France (IUF), 1 rue Descartes, 75231 Paris Cedex 05, France*

(Received 29 April 2020; accepted 9 October 2020; published 6 November 2020)

We examine the steady state and dynamic behavior of an optical resonator comprised of two interlinked fiber loops sharing a common pump. A coupled Ikeda map models with great accuracy the field evolution within and exchange between both fibers over a single round trip. We find this supports a range of rich multidimensional bistability in the continuous wave regime, as well as previously unseen cavity soliton states. Floquet analysis reveals that modulation and parametric instabilities occur over wider domains than in single-fiber resonators, which can be tailored by controlling the relative dispersion and resonance frequencies of the two fiber loops. Parametric instability gives birth to a train of pulses with a peculiar period-doubling behavior.

DOI: 10.1103/PhysRevResearch.2.043195

I. INTRODUCTION

Optical resonators are complex physical platforms, exhibiting an even richer range of phenomena than single-pass nonlinear systems due to their driven-dissipative nature. They are of increasing importance in metrology as sources of highly tunable, broadband frequency combs [1–3]. The Kerr cavity soliton is one of the fundamental states responsible for generating these combs [4–8]. Further, they have been proposed as cryptographic tools due to their chaotic output [9–11]. Nonlinear optical resonators can be precisely modelled by the so-called Ikeda map [12,13], which describes separately the evolution of the electric field as it propagates through the cavity, and the boundary conditions which account for the injection of pump light and transmission of the cavity field between each round trip.

In this work, we propose a resonator composed of two fiber loops sharing a common pump. This geometry is reminiscent of the Möbius strip. Indeed, the two fiber coils are not closed, but they form a unique loop, in the same way as a Möbius surface has a unique side. The structure of the Möbius fiber resonator we consider is shown in Fig. 1. We model the light propagation inside this resonator by means of a coupled Ikeda map. Several works have considered extended/multidimensional Ikeda maps and mean-field approximations by Lugiato-Lefever equations with nonlinear coupling between the fields of a single resonator [14–21]. Xue *et al.* [22] examine the nonlinear response of a similar fiber resonator with weakly coupled loops, showing how Kerr cavity solitons may be generated with great efficiency in one fiber loop by weakly coupling to a much shorter loop driven with a constant pump field. While their extended mean-field model could be applied to the Möbius resonator, we choose to study the full Ikeda map as we work with a wide variety of conditions often far from resonances. Here mean-field models may be less accurate [7] unless several resonances are included [23]. For our purposes, limiting ourselves to Möbius resonators composed of two identical-length loops, the Ikeda map is generally straightforward and realistic to apply.

The dimensionless Ikeda map connecting the fiber fields between round trips (labelled with an integer m) is

$$\begin{aligned} A_1^{m+1}(z=0,t) &= \sqrt{\theta}A_{\text{in}} + \sqrt{1-\theta}e^{-i\delta_2}A_2^m(z=1,t), \\ A_2^{m+1}(z=0,t) &= \sqrt{\theta}A_{\text{in}} + \sqrt{1-\theta}e^{-i\delta_1}A_1^m(z=1,t), \end{aligned} \tag{1}$$

while intrafiber propagation is described by a lossy nonlinear Schrödinger equation (NLSE)

$$i\partial_z A_n^m = \eta_n \partial_t{}^2 A_n^m + i\beta_{3,n}\partial_t{}^3 A_n^m - \left|A_n^m\right|^2 A_n^m - i\frac{\alpha_i}{2}A_n^m. \tag{2}$$

for fibers indexed as $n = 1, 2$. We work in dimensionless units in which the intrafiber propagation coordinate $z = \tilde{z}/L$ is scaled to the common fiber length L (denoting here and subsequently all physical counterparts of dimensionless quantities with a tilde $\sim$). By assuming identical length fiber loops, we neglect the possibility of temporal walk-off between pulses traveling through either fiber. This loss in our model's generality is compensated by its simplicity and ease of numeric integration for our case compared to multiresonance schemes. Time $t = \tilde{t}\sqrt{2/|\beta_{2,2}|L}$ is scaled by the second-order dispersion coefficient of the second fiber $\beta_{2,2} \equiv [\partial_\omega^2\beta_2]_{\omega_0}$, given propagation constant (wave number) $\beta_2(\omega)$ in the second fiber and pump frequency ω_0. Hence $\eta_2 \equiv \text{sgn}(\beta_{2,2})$ and $\eta_1 = \text{sgn}(\beta_{2,1})|\beta_{2,1}/\beta_{2,2}|$ and the dimensionless third order dispersion parameters are related to their physical

*cm350@hw.ac.uk

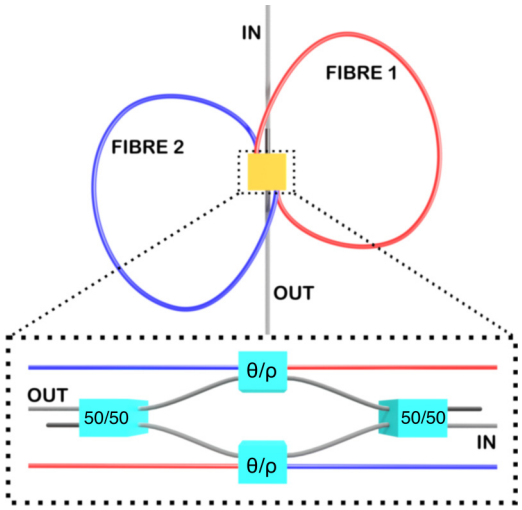

FIG. 1. Schematic of the Möbius fiber loop resonator. A pair of optical fibers (red and blue) are linked as shown, such that the output of each is fed into the other's input. The gold region is expanded inside the dashed box to reveal the coupling structure within; pump light is split equally by a 50/50 coupler to provide a common input to both loops in the resonator. Ikeda boundary conditions are implemented by couplers whose ratios are θ to $\rho \equiv 1-\theta$. Outputs from both resonators together with reflected pump light are recombined by a second 50/50 coupler. Short black fibers represent redundant coupler ports which are not used.

counterparts $\beta_{3,n} = \sqrt{2/|\beta_{2,2}|^3 L}[\partial_\omega^3 \beta_n]_{\omega_0}/3$. The fiber fields A_n^m are related to physical electric fields as $A_n^m = \sqrt{\gamma L}\tilde{A}_n^m$, where γ is the Kerr nonlinear coefficient, and similarly the pump field $A_{\rm in} = \sqrt{\gamma L}\tilde{A}_{\rm in}$. Since we work with a pump which is implicitly a time-independent constant, our frequency variable Ω expresses a scaled detuning of the physical frequency ω from ω_0, that is $\Omega = (\omega - \omega_0)\sqrt{|\beta_{2,2}|L/2}$. θ parametrizes the transmission of pump light into the fibers and fiber output fields into the bus waveguide. The absorption coefficient is also scaled by the fiber length $\alpha_i = \tilde{\alpha}_i L$, while the detunings $\delta_n = 2k\pi - \beta_n(\omega_0)L$ measure the phase difference accumulated per round trip with respect to the nearest single-loop resonance indexed by the integer k.

In this paper, we investigate the power within the fibers of the Möbius resonator in different dynamical situations. First we examine steady states in the continuous-wave (time independent) limit, where the field in either fiber is independent of both the round trip number n and the intracavity time coordinate t. This reveals an extended set of solutions exhibiting bistability, whose symmetry depends on the relative detuning of the two fiber loops. In the following section, we consider the dynamical case in which the fiber fields vary over time, but periodically repeat themselves within both loops after one or more resonator round trips, defining a (dynamical) steady state. Here, allowing the fiber loops to have different dispersive characteristics gives rise to a new class of Kerr cavity solitons. The structure of these solitons is sensitive to the relative second- and third-order dispersion coefficients in each fiber. Finally, we derive the modulation instability (MI) spectrum by applying Floquet analysis, which demonstrates the existence of additional Arnold instability tongues beyond those found in single fiber resonators, arising from dispersion variations between the two loops.

II. HOMOGENEOUS STEADY STATES

We first seek the time-independent steady states of the Ikeda map in both fiber loops. For simplicity, here we work in the low α_i limit, such that we incorporate round trip losses into the Ikeda boundary conditions $\sqrt{\tilde{\rho}} = \sqrt{1-\theta}\exp(-\alpha_i/2)$ and the power within each fiber remains constant over a single round trip. A pair of equations for the steady state fields is obtained by first integrating the NLSE Eq. (2) over one round trip, giving $A_n^m(z=1) = \exp(i|A_n^m(z=0)|^2)A_n^m(z=0)$. Using this, we substitute for $A_n^m(1)$ in Eq. (1), imposing the constraint $A_n^{m+1}(0) = A_n^m(0)$. Substituting for one field in each equation using the other's expression and vice versa, then multiplying on either side of both by their complex conjugates, yields two simultaneous equations for the intrafiber powers $Y \equiv |A_1|^2$, $Z \equiv |A_2|^2$:

$$\begin{aligned}(1+\tilde{\rho}^2 - 2\tilde{\rho}\cos(Y+Z-\delta_1-\delta_2))Y \\ = (1+\tilde{\rho}+2\sqrt{\tilde{\rho}}\cos(Z-\delta_2))\theta X, \\ (1+\tilde{\rho}^2 - 2\tilde{\rho}\cos(Y+Z-\delta_1-\delta_2))Z \\ = (1+\tilde{\rho}+2\sqrt{\tilde{\rho}}\cos(Y-\delta_1))\theta X. \end{aligned} \tag{3}$$

A single equation for Y and Z can be obtained from these by eliminating the common pump term θX:

$$\begin{aligned} Y(1+\tilde{\rho}+2\sqrt{\tilde{\rho}}\cos(Y-\delta_1)) \\ = Z(1+\tilde{\rho}+2\sqrt{\tilde{\rho}}\cos(Z-\delta_2)). \end{aligned} \tag{4}$$

Some example plots of solutions to Eq. (4) with a fixed δ_2 and various δ_1 are shown in Fig. 2. Red and blue sections indicate unstable and stable solution branches, respectively. The general structure of the curves repeats periodically in both Y and Z directions. We determine stability by performing a Floquet analysis around solutions in the limit of zero frequency; a solution is stable if and only if the modulus of the Floquet matrix's eigenvalues are less than unity. The general, frequency-dependent version of this Floquet theory is presented in Sec. IV. In the case of a resonator with equivalent fibers, $\delta_1 = \delta_2$, the powers follow a symmetric bistability curve similar to that in Fig. 1(a) in Ref [24]. If the fibers are unequally detuned however, the curve opens asymmetrically. If the detuning imbalance between the two fibers is relatively small, a separate closed orbit exists, close to which the solutions approximate an elliptic curve [25]. These approximate local elliptic curves are indicated by dashed boxes in Fig. 2. Although in the present paper we do not explore the implications of the existence of such curves in the stationary state diagram (a unique feature of our Möbius resonators), it is interesting to notice that elliptic curves are widely used in practical cryptography due to their amazingly rich group-theoretical structure that allows for efficient factoring of large integers [26,27]. One could easily speculate that optical systems could be well-suited to study empirically open number-theoretical problems such as the famous Birch and Swinnerton-Dyer

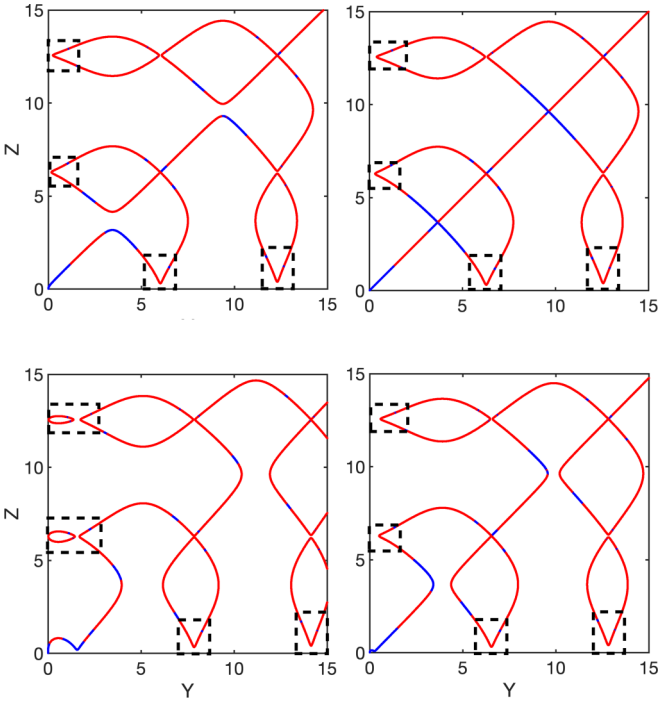

FIG. 2. Solutions to Eq. (4) showing the possible stationary state powers Y, Z in the first and second fiber, respectively, given fixed $\delta_2 = \pi$ and different values of δ_1, increasing sequentially through $11\pi/12$, π, $13\pi/12$, and $3\pi/2$ going clockwise from top left to bottom left. The stable and unstable solutions are marked by blue and red points, respectively. Those which approximate sections of elliptic curves lie in the regions enclosed by the dashed boxes. Here $\theta = 2/15$ and $\alpha_i = 0$.

conjecture [28]. At higher pump powers, the fields do not converge to round trip independent constants and either chaotic or cyclic patterns may emerge, as may be inferred by the relatively low fraction of stable solutions in Fig. 2. The latter may exhibit period-doubling behavior, on which we will elaborate in Sec. IV.

III. DYNAMIC STEADY STATES & MÖBIUS CAVITY SOLITONS

If the two fibers have identical parameters and detuning, we recover the typical regimes of ring resonator steady state behavior, which are well described in the mean-field limit by a Lugiato-Lefever equation [5]. These are illustrated in Fig. 3, which shows a sequence of homogeneous, modulation instability, chaotic, oscillating and stabilized cavity solitons followed finally by homogeneous steady states as the detuning of both fibers is gradually increased over the resonant interval. Here and in all that follows, the intracavity states given varying values of detuning $\delta_1 = \delta_2$ are recorded after propagating the initial condition over many round trips of the dual Ikeda map Eq. (1). Specifically, at each step we increment $\delta_1 = \delta_2$ by a small amount and propagate over 500 round trips, using the output from the previous $\delta_1 = \delta_2$ increment as the initial condition. We also add noise signals with each increment to both fibers $A_n(t) \to A_n(t) + a\exp(i\psi_n(t))$, with a set as one tenth of the initial pulse amplitude and the phase

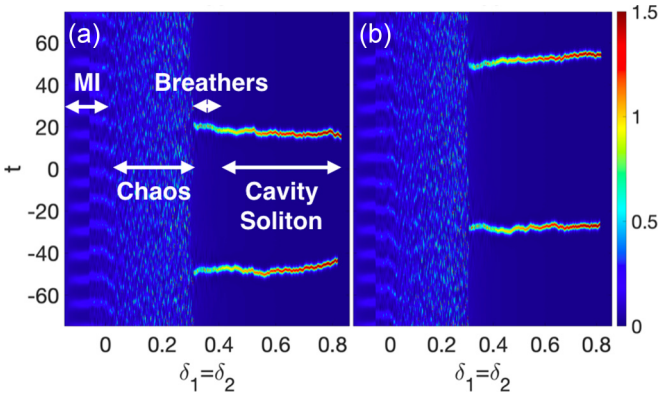

FIG. 3. Stationary state power distributions Y_{SS} in fiber 1 (a) and Z_{SS} in fiber 2 (b) over time which emerge in a Möbius resonator composed of two identical fibers, as a function of common detuning from the pump $\delta_1 = \delta_2$. The steady states are obtained by sequentially incrementing both δ_1 and δ_2 in steps of 0.01, then propagating for 500 round trips of the dual Ikeda map Eq. (1). Parameters: $A_{\rm in} = 0.166$, $\beta_{3,n} = 0$, $\eta_1 = \eta_2 = -1$, $\theta = 2/15$, and $\alpha_i = 1/100$. Different regimes of dynamic steady-state behavior are indicated with white labels and arrows; the steady state is time-independent for detunings outside these ranges.

ψ being randomized for each point in time, independently for both fields. The purpose of this is to ensure that the steady state we converge to is robust. This is typically sufficient to obtain convergence to the steady state in each case. At the first integration step we choose the initial condition $A_n(t) = 1.2\,\mathrm{sech}(1.2t)$ for $n = 1, 2$. We also choose $A_{\rm in} = 0.166$, $\theta = 2/15$, and $\alpha_i = 1/100$.

The two fibers within the loop may have completely different dispersive properties. In the first example, we examine the steady states within a fiber resonator, where one fiber has normal dispersion $\eta_2 = +1$, while the other has stronger anomalous dispersion $\eta_1 = -1.5$. Surprisingly similar behavior regimes to those seen with identical anomalous fibers emerge, with clear transitions from stationary MI patterns to chaos followed by cavity soliton formation (Fig. 4). When multiple solitons form collisions may occur; at lower detuning this results in the solitons merging, whereas they tend to

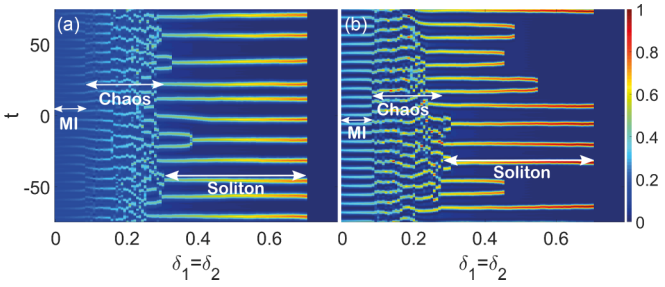

FIG. 4. Stationary state power distributions Y_{SS} in fiber 1 (a) and Z_{SS} in fiber 2 (b) over time which emerge in a Möbius resonator composed of one anomalously dispersive fiber $\eta_1 = -1.5$ and a second, normally dispersive fiber $\eta_2 = 1$, as a function of common detuning from the pump $\delta_1 = \delta_2$. No third-order dispersion is present; parameters are $A_{\rm in} = 0.166$, $\beta_{3,n} = 0$, $\theta = 2/15$, and $\alpha_i = 1/100$.

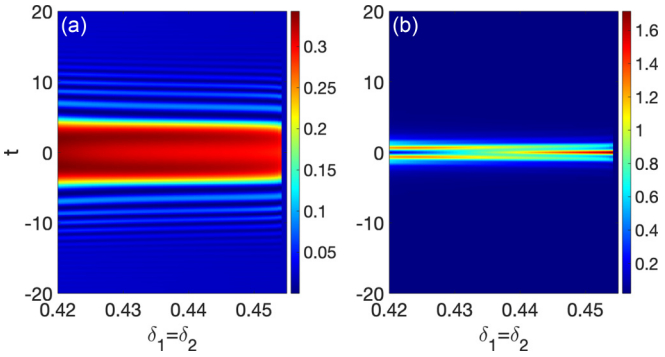

FIG. 5. Stationary state power distributions Y_{SS} in fiber 1 (a) and Z_{SS} in fiber 2 (b) over time, which emerge in a Möbius resonator composed of fibers with opposite group velocity dispersion (GVD) $\eta_1 = -\eta_2 = -1$ but otherwise identical parameters, as a function of common detuning from the pump $\delta_1 = \delta_2$.

collapse for higher detuning. Reducing the strength of the anomalous dispersion in the second fiber decreases the detuning ranges for which MI and cavity solitons are supported.

Considering a pair of fibers which have equal and opposite dispersion, $\eta_1 = -\eta_2 = -1$, neither modulation instability nor chaotic steady states emerge. However, instead of the usual Kerr cavity soliton, a new kind of compact state which we term *Möbius cavity soliton* (MCS) appears with a complicated yet stable waveform in the fields of both fibers. Figure 5 plots the intracavity power from both fibers as a function of detuning. The MCS appears only within a small detuning range $\delta \in (0.42, 0.455)$, and its structure changes somewhat within this. Outside of this range only homogeneous steady states appear, with the modulation instability and chaotic regimes apparently suppressed. On closer examination, plotting the field's intrafiber evolution over two round trips reveals that the stationary fields are snapshots of a stable periodic state which oscillates smoothly between the two (Fig. 6). The periodic behavior arises as the field experiences cyclic second-order dispersion as it travels through both loops of the resonator; a similar state was previously found in a dispersion-modulated fiber ring [29]. The spectrum of this MCS is considerably wider than that of the standard cavity soliton given the same pump power and detuning, and therefore is a promising seed for a broadband frequency comb when emitted in a pulse train.

Including third order dispersion $\beta_{3,n} = 2.6$ in both fibers, the MCS becomes asymmetric in time and acquires a finite group velocity. It is stable for an extended detuning range $\delta \in (0.34, 0.45)$, however unlike the previous MCS which results from $\beta_{3,n} = 0$ the two fields within the resonator are distinct and do not periodically transform into each other. As a consequence the intracavity field in either fiber swaps each round trip (but appears stationary when examined every second round trip). From this, it is clear that the initial condition affects steady state stability, as the field which first traveled through the anomalously-dispersive fiber supports a MCS to a slightly larger detuning limit than that which started in the fiber with normal dispersion. This MCS has a highly oscillatory structure in time and a narrower, peaked spectrum with resonant radiation resulting from the third-order

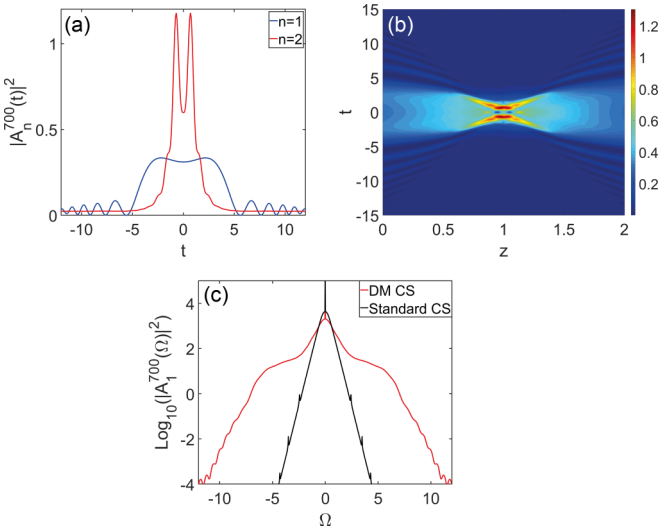

FIG. 6. Example of the intracavity steady state power in a Möbius resonator composed of two fibers with equal and opposite second-order dispersion $\eta_1 = -\eta_2 = -1$. Both fibers are detuned from the pump by $\delta_1 = \delta_2 = 0.43$. (a) Intracavity power profiles from fiber one and fiber two after 700 round trips. (b) Power profile over time resulting from intrafiber propagation of one field over two round trips, showing how the state continuously changes from the distribution in one fiber to the other and back over one period of the Möbius cavity soliton (MCS). (c) Comparison of the MCS spectrum with that of a standard Kerr cavity soliton which forms in an equivalent resonator with fibers that have the same dispersion, given the same pumping and initial condition as the dispersion oscillating resonator. The MCS bandwidth is considerably larger, particularly at lower powers.

dispersion clearly visible (Fig. 7). There are multiple peaks as the Ikeda boundary conditions result in a series of possible phase-matched wave numbers rather than one [30,31]; these appear to satisfy phase matching conditions for integers k

$$\langle \beta_{3,n} \rangle \Omega^3 + \langle \eta_n \rangle \Omega^2 = \langle \delta_n \rangle + \tfrac{1}{2} \langle P_n \rangle + 2\pi k \qquad (5)$$

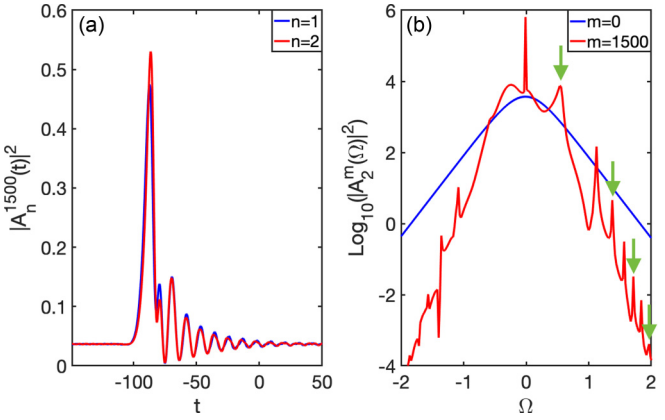

FIG. 7. (a) Power profiles from fiber one and fiber two given $\delta = 0.36$, $\eta_1 = -\eta_2 = -1$ and $\beta_{3,1} = \beta_{3,2} = 2.6$. (b) Comparison of the MCS spectrum with that of the input pulse. The green arrows indicate the resonant radiation peaks. The other peaks result from four-wave mixing between these.

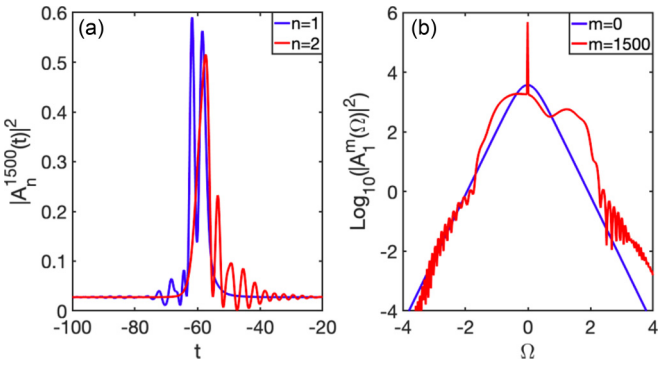

FIG. 8. (a) Power profiles from fiber one and fiber two given $\delta = 0.4$, $\eta_1 = -\eta_2 = -1$ and $\beta_{3,1} = -\beta_{3,2} = 2.6$. (b) Comparison of the MCS spectrum with that of the input pulse.

where $\langle\rangle$ denotes the averaging of a parameter over the fiber index n and P_n is the peak power of the soliton in fiber n. Note that in the case of Fig. 7 $\langle\eta_n\rangle = 0$ and there is only one positive-frequency root for each k. We assume the other peaks in the spectrum result from four-wave mixing between these phase-matched frequencies. If the sign of $\beta_{3,n}$ swaps between fibers as well that of η_n, a similar MCS forms in both fiber loops. The oscillating $\beta_{3,n}$ leads to a reduced MCS group velocity compared to the state formed with a common $\beta_{3,n}$ as well as a reversed t-asymmetry between the intracavity power (Fig. 8). Further, clear resonant radiation spectral peaks do not appear since consistent phase-matching cannot be achieved under these conditions. Specifically, $\langle\beta_{3,n}\rangle = \langle\eta_n\rangle = 0$ so Eq. (5) cannot be satisfied for any Ω.

Allowing for unequal detuning from resonance in the two fibers $\delta_1 \neq \delta_2$ adds an additional dimension to the resonator's parameter space and considerably extends the possible existence of dynamical steady states. Performing a similar survey of time dependent steady states over $(\delta_1, \delta_2) \in [-\pi, \pi] \times [-\pi, \pi]$ as was done in Fig. 3 for a resonator with $\eta_1 = -1.5$, $\eta_2 = 1$ yields a map as shown in Fig. 9. Time dependent states are concentrated around the joint resonance close to the line $\delta_1 + \delta_2 = 0$. Proceeding from the negative $(-\pi, -\pi)$ to positive (π, π) extremes of detuning we find the familiar sequence of homogeneous, modulationally unstable, chaotic, solitonic and homogeneous states. These state domains show some curvature in the (δ_1, δ_2) plane, which we expect to increase with pump power and round trip losses.

We note that the dynamical steady-states are dependent on the sequence of parameters tested and their initial values. For example, if the scan of increasing detuning shown in Fig. 5 had started with $\delta_1 = \delta_2 = 0.4$, the corresponding steady state would be homogeneous. On increasing $\delta_1 = \delta_2$ from this point, we would not observe the formation of Möbius solitons in the same detuning range unless an external perturbation was added. It appears that the chaotic MI phase from which cavity solitons typically emerge is suppressed in resonators with $\eta_1 = -\eta_2 = -1$, meaning they will not appear spontaneously on increasing detuning from the homogeneous state. Likewise, had we examined the same detuning ranges in reverse order a different sequence of states would result. This dependence would be considerably more complicated to explore in a higher-dimensional plot such as Fig. 9, where there are many more starting points and directions in detuning space from which to probe the resonance. The analysis of bifurcation, hysteresis and multi-stability in single fiber resonators is a complex area of study in itself [32–34], so we propose a more thorough examination of these as applied to the Möbius resonator in future works.

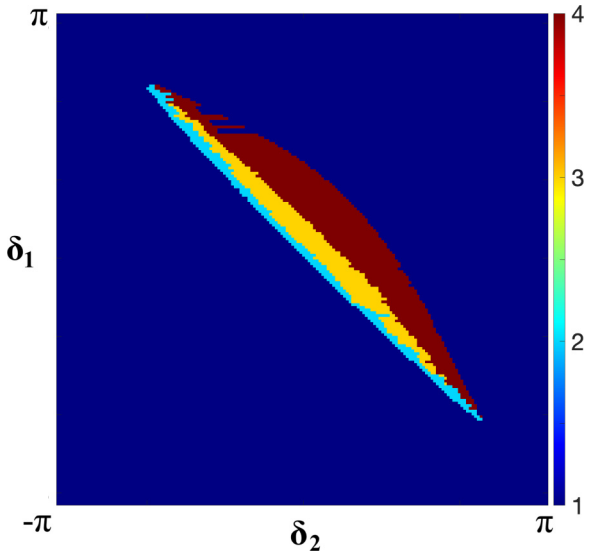

FIG. 9. Dynamical steady-state category in fiber 1 as a function of fiber detunings from resonance (δ_1, δ_2). States are identified by a color code; homogeneous states 1, modulation instability 2, chaotic states 3, and cavity solitons 4.

IV. MODULATION INSTABILITY

The presence of two fibers in the resonator with distinct dispersive properties raises the possibility of strongly modified modulation instability compared with that observed in homogeneous fiber resonators [7,35,36]. The stepwise dispersion modulation seen by light over a complete round trip of the resonator might be expected to result in similar instabilities as a resonator composed of a single fiber with oscillating dispersion, as presented in several previous works [37–40]. To investigate this, we adapt the Floquet analysis of Ref. [38] to the Möbius resonator. The only significant extension required is that perturbations in both fibers must be monitored simultaneously to describe a complete round trip, meaning we have a system of four simultaneous equations to solve rather than two. To facilitate analysis, we incorporate small round trip losses as in Sec. II into the boundary condition of the Ikeda map (1), which now reads

$$A_1^{m+1}(z=0,t) = \sqrt{\theta}A_{\text{in}} + \sqrt{\tilde{\rho}}e^{-i\delta_2}A_2^m(z=1,t),$$
$$A_2^{m+1}(z=0,t) = \sqrt{\theta}A_{\text{in}} + \sqrt{\tilde{\rho}}e^{-i\delta_1}A_1^m(z=1,t), \quad (6)$$

$$\partial_z A_n^m = -i\eta_n \partial_t{}^2 A_n^m + i\left|A_n^m\right|^2 A_n^m \quad (7)$$

with $\tilde{\rho} + \theta < 1$. We write the total field in the two resonators as $A_1^m(z,t) = \overline{A}_1 + \breve{a}^m(z,t) + i\breve{b}^m(z,t)$, $A_2^m(z,t) = \overline{A}_2 + \breve{c}^m(z,t) + i\breve{d}^m(z,t)$. $\breve{a}, \breve{b}, \breve{c}, \breve{d}$ are real perturbations and the time-independent stationary state in resonator n is

$$\overline{A}_n(z) = \sqrt{P_n}\exp(iP_n z + \psi_n). \quad (8)$$

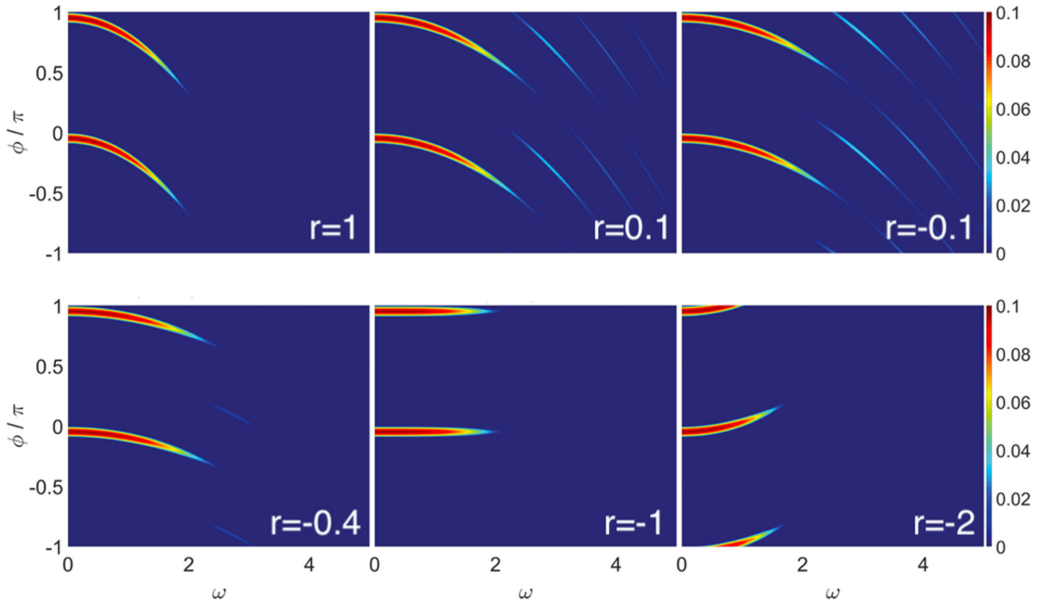

FIG. 10. Modulation instability gain as a function of frequency ω and common round trip phase $\phi_1 = \phi_2 = \phi$ for various ratios of second-order dispersion $r \equiv \eta_2/\eta_1$ in the two resonator fibers.

As discussed earlier, there is no analytic solution available for the steady state powers P_n and phases ψ_n, though it is straightforward to find them numerically by integrating a time-independent version of the Ikeda map. Considering solely evolution through the first fiber loop, the linearized NLSE for the perturbation coefficients reduces to a 2×2 coupled pair of ordinary differential equations,

$$\frac{d}{dz}\begin{pmatrix} a^m(z,\omega) \\ b^m(z,\omega) \end{pmatrix} = \begin{pmatrix} 0 & -\eta_1\omega^2 \\ \eta_1\omega^2 + 2P_1 & 0 \end{pmatrix}\begin{pmatrix} a^m(z,\omega) \\ b^m(z,\omega) \end{pmatrix}. \quad (9)$$

Note the perturbations have been Fourier transformed into the frequency (ω) domain. This problem has solutions with eigenvalues

$$\pm k_1 = \pm\sqrt{\eta_1\omega^2(\eta_1\omega^2 + 2P_1)} \quad (10)$$

and corresponding eigenvectors

$$\mathbf{v}_{+,-} = \begin{pmatrix} \cos(k_1 z) \\ \frac{k_1}{\eta_1\omega^2}\sin(k_1 z) \end{pmatrix}, \begin{pmatrix} -\frac{\eta_1\omega^2}{k_1}\sin(k_1 z) \\ \cos(k_1 z) \end{pmatrix}. \quad (11)$$

The eigenvectors define a fundamental solution matrix for the ODE (9) $X_1(z) = (\mathbf{v}_+, \mathbf{v}_-)$. A completely analogous solution matrix will exist for the perturbations in the second

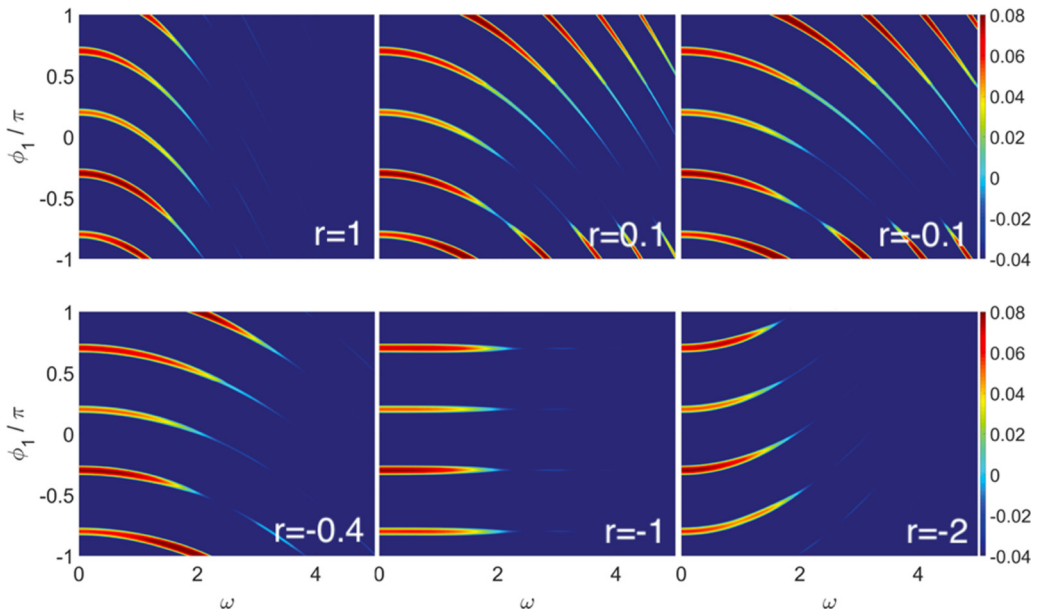

FIG. 11. Modulation instability gain as a function of frequency ω and round trip phase in the first fiber $\phi_1 = \phi_2 - \pi/2$ for various ratios of second-order dispersion $r \equiv \eta_2/\eta_1$ in the two resonator fibers.

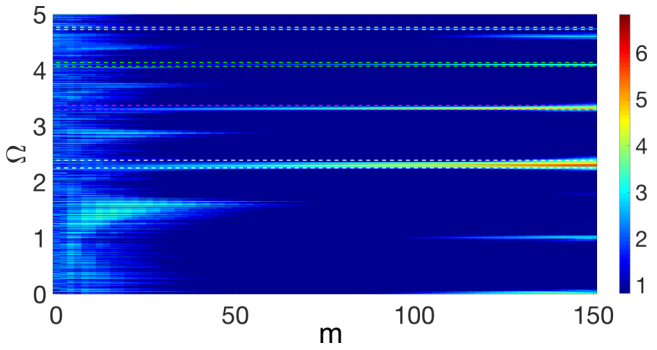

FIG. 12. Modulation instability spectrum that emerges over m round trips in a Möbius resonator with $\delta_1 = \delta_2 = 0.6\pi$, $P_1 = P_2 = 0.2$, and $\eta_2 = 10\eta_1 = 1$. Colour axis shows the intracavity spectral power of the second fiber on a logarithmic scale, as measured every second round trip. Only the positive half of the spectrum is shown since it is symmetric about $\Omega = 0$. The spectrum in the first fiber loop is nearly identical and features sidebands with the same strength and position as those shown here. Dashed white, magenta, green, and yellow lines indicate the band edges as predicted by the instability gain spectrum resulting from Floquet analysis.

fiber;

$$X_2(z) = \begin{pmatrix} \cos(k_2 z) & -\frac{\eta_2\omega^2}{k_2}\sin(k_2 z) \\ \frac{k_2}{\eta_2\omega^2}\sin(k_2 z) & \cos(k_2 z) \end{pmatrix}. \tag{12}$$

These can be combined into a single 4×4 block diagonal matrix which describes the evolution of all perturbations in the $\mathbf{a}^m(z) = (a^m, b^m, c^m, d^m)$ basis as

$$X(z_1, z_2) = \left[\begin{array}{c|c} X_1 & O_2 \\ \hline O_2 & X_2 \end{array}\right] \tag{13}$$

given O_2 is the 2×2 null matrix. Meanwhile the boundary conditions can be implemented by a combined rotation

$$\Gamma = \sqrt{\tilde{\rho}}\left[\begin{array}{c|c} O_2 & \Gamma_2 \\ \hline \Gamma_1 & O_2 \end{array}\right], \tag{14}$$

where

$$\Gamma_n = \begin{pmatrix} \cos(\phi_n) & -\sin(\phi_n) \\ \sin(\phi_n) & \cos(\phi_n) \end{pmatrix} \tag{15}$$

and $\phi_1 = P_1 - \delta_1 + \psi_1 - \psi_2$, $\phi_2 = P_2 - \delta_2 + \psi_2 - \psi_1$. The combined matrix describing a complete round trip evolution is the product of these, $W = \Gamma X(1, 1)$. The eigenvalues and eigenvectors of W can be solved for analytically, however the expressions are not particularly tractable. The four eigenvalues consist of two pairs with equal magnitudes but opposite sign, $\pm\lambda_1, \pm\lambda_2$; since the eigenvalue modulus is what determines instability gain, we need only consider one of each pair. The gain for a particular frequency ω is then [38]

$$g(\omega) = \ln\left(\max(|\lambda_1(\omega)|, |\lambda_2(\omega)|)\right). \tag{16}$$

We plot the gain assuming different values of dispersion in both fibers in Fig. 10, assuming the detuning in both fibers is the same. At least two instability branches are always present at low frequencies. Increasing the GVD value in the first fiber η_1 relative to the fixed GVD in the second fiber $\eta_2 = 1$ alters the curvature of the instability branches; it also gives rise to two additional branches at higher frequencies when the difference in dispersion magnitude between the two fibers is sufficiently big. This is consistent with the findings of Ref. [38].

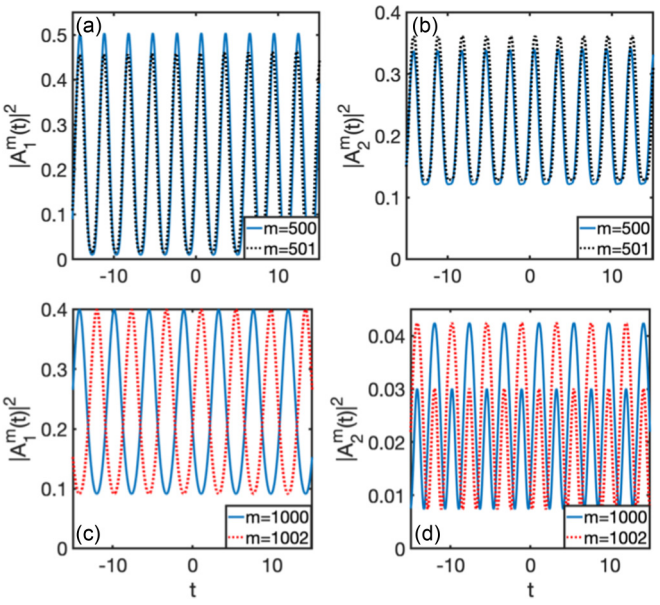

FIG. 13. Intracavity power over time in fiber one [(a) and (c)] and fiber two [(b) and (d)] after m round trips. In (a) and (b), $\delta_1 = \delta_2 = \pi$, which results in a single P1 instability branch being excited. As the eigenvalues of the Floquet matrix W are real, the MI pattern repeats exactly in both fibers every second round trip, i.e., $A_n^m(t) = A_n^{m+2}(t)$. In contrast, for (c,d) $\delta_1 = \pi$ and $\delta_2 = \pi/2$, which leads to a Faraday P2 MI branch being excited. Imaginary Floquet eigenvalues leads to period doubling, which manifests as a repetition of the Faraday MI pattern within each fiber every two round trips, with the phase of the pattern reversing each time. Hence four round trips are necessary for a complete cycle $A_n^m(t) = A_n^{m+4}(t)$. Other parameters: $|A_{\text{in}}|^2 = 1.79$, $\eta_1 = 10\eta_2 = 1$, and $\theta = 2/15$.

Here we have an additional degree of freedom in the relative detuning between the two fibers, which can modify the both the extent and positions of the branches. For example, choosing $\phi_2 = \phi_1 + \pi/2$ leads to the modified gain in Fig. 11, which shows the branches enabled by dispersion oscillation in Fig. 10 become significant at low frequencies for any relative dispersion η_1/η_2. It is interesting to note that when the two loops have dispersion with equal magnitude but opposite signs, the instability branches become flat. This means that for each steady state parametrized by the phase ϕ, either we have no gain, or the gain is peaked around $\omega = 0$. Hence the steady state is either stable or unstable with respect to zero frequency perturbations, that is the unstable state of a multistable response. This fact explains why no modulation instability is observed for opposite dispersions, as we found in the previous section (see Fig. 5).

To check the accuracy of the Floquet analysis' predictions we numerically simulate MI in a Möbius resonator with $\delta_1 = \delta_2 = 0.6\pi$, $P_1 = P_2 = 0.2$, and $\eta_1 = 10\eta_2 = 1$. The Floquet theory indicates that to first order there should be four pairs

of instability bands under these conditions, and indeed the numerically integrated spectrum shows three sidebands developing after 100 round trips (see Fig. 12).

Instability branches may vary in their period behavior; MI patterns on certain branches repeat exactly after every two round trips, whereas those on others repeat every four round trips. The period-doubling behavior associated with Faraday-type instability branches is well documented in other works [7,38,40]; an example is presented in Figs. 13(c) and 13(d), in which the intracavity power in either fiber shows the same MI pattern after two round trips, but exactly out-of-phase with respect to the original pattern. The power time series in both fibers repeats exactly every four round trips, corresponding to a full period of the Faraday instability. This contrasts with homogeneous or dispersion oscillating cavities, where the Faraday instability gives rise to a period two pattern. This periodicity is explained by the fact that the unstable eigenvalues of the Floquet matrix W are purely imaginary over these branches, i.e., they have a phase of $\pm\pi/2$. The perturbations are again in-phase after four round trips, which eventually generates the observed sequence. For comparison an instability pattern that develops with real Floquet eigenvalues, which repeats exactly every two round trips, is presented in Figs. 13(a) and 13(b). A detailed analysis of parametric instabilities of the Möbius resonator and they period doubling is outside the scope of this paper and it will be reported elsewhere.

V. CONCLUSION

We have found new dissipative structures in a Möbius optical fiber resonator, which to our knowledge has not been studied previously. When continuous-wave solutions are modulationally stable, their powers define unusual bistability curves which may be approximated by elliptic curves in certain limits. A variety of time-dependent localized and periodic states which cannot be realized by standard fiber resonators are supported, including exotic cavity solitons and extended modulation instability. These are enabled by the ability to tune the resonances and dispersive properties of both fibers in the resonator independently. We anticipate that Möbius cavity solitons will be of interest to researchers working on frequency comb generation, owing to their broadened spectrum compared to the typical Kerr cavity soliton.

ACKNOWLEDGMENTS

C.M. acknowledges studentship funding from Engineering and Physical Sciences Research Council (EPSRC) under CM-CDT Grant No. EP/L015110/1. F.B. acknowledges support from the German Max Planck Society for the Advancement of Science (MPG), in particular the IMPP partnership between Scottish Universities and MPG. We thank our anonymous reviewer for their constructtive input, which has improved the quality of this manuscript.

[1] P. Del'Haye, A. Schliesser, O. Arcizet, T. Wilken, R. Holzwarth, and T. J. Kippenberg, Nature (London) **450**, 1214 (2007).
[2] T. J. Kippenberg, R. Holzwarth, and S. A. Diddams, Science **332**, 555 (2011).
[3] A. Schliesser, N. Picqué, and T. W. Hänsch, Nat. Photonics **6**, 440 (2012).
[4] F. Leo, L. Gelens, P. Emplit, M. Haelterman, and S. Coen, Opt. Express **21**, 9180 (2013).
[5] S. Coen and M. Erkintalo, Optics Lett. **38**, 1790 (2013).
[6] T. Herr, V. Brasch, J. D. Jost, C. Y. Wang, N. M. Kondratiev, M. L. Gorodetsky, and T. J. Kippenberg, Nat. Photonics **8**, 145 (2014).
[7] T. Hansson and S. Wabnitz, J. Opt. Soc. Am. B **32**, 1259 (2015).
[8] R. Bitha and A. M. Dikandé, Eur. Phys. J. D **73**, 152 (2019).
[9] R. V. Ramos and R. F. Souza, Microwave Opt. Technol. Lett. **24**, 79 (2000).
[10] Y. Imai, S. Yamauchi, H. Yokota, T. Suzuki, and K. Tsuji, Opt. Commun. **282**, 4141 (2009).
[11] S. Tunsiri *et al.*, Procedia Eng. **32**, 475 (2012).
[12] K. Ikeda, Opt. Commun. **30**, 257 (1979).
[13] G. Steinmeyer, A. Buchholz, M. Hänsel, M. Heuer, A. Schwache, and F. Mitschke, Phys. Rev. A **52**, 830 (1995).
[14] G. D'Aguanno and C. R. Menyuk, Phys. Rev. A **93**, 043820 (2016).
[15] G. D'Aguanno and C. R. Menyuk, Eur. Phys. J. D **71**, 74 (2017).
[16] X. Yi, Q.-F. Yang, X. Zhang, K. Y. Yang, X. Li, and K. Vahala, Nat. Commun. **8**, 14869 (2017).
[17] H. Guo, E. Lucas, M. H. P. Pfeiffer, M. Karpov, M. Anderson, J. Liu, M. Geiselmann, J. D. Jost, and T. J. Kippenberg, Phys. Rev. X **7**, 041055 (2017).
[18] M. T. M. Woodley, J. M. Silver, L. Hill, F. Copie, L. Del Bino, S. Zhang, G.-L. Oppo, and P. Del'Haye, Phys. Rev. A **98**, 053863 (2018).
[19] M. Haelterman, Appl. Phys. Lett. **61**, 2756 (1992).
[20] M. Haelterman, Opt. Lett. **17**, 792 (1992).
[21] M. Haelterman, Opt. Commun. **100**, 389 (1993).
[22] X. Xue, X. Zheng, and B. Zhou, Nat. Photonics **13**, 616 (2019).
[23] M. Conforti and F. Biancalana, Opt. Lett. **42**, 3666 (2017).
[24] L. Hill, G.-L. Oppo, M. T. M. Woodley, and P. Del'Haye, Phys. Rev. A **101**, 013823 (2020).
[25] L. C. Washington, *Elliptic Curves: Number Theory and Cryptography* (Chapman and Hall/CRC Press LLC, Boca Raton FL, 2003).
[26] W. Stein, *Elementary Number Theory: Primes, Congruences, and Secrets*, Undergraduate Texts in Mathematics (Springer-Verlag, New York, 2009), Vol. 106.
[27] H. W. Lenstra, Ann. of Math. **126**, 649 (1987).
[28] W. Stein, *Rational Points on Elliptic Curves*, Undergraduate Texts in Mathematics (Springer-Verlag, New York, 1992), Vol. 74.
[29] A. Gavrielides and B. A. Malomed, Opt. Commun. **241**, 51 (2004).
[30] J. K. Jang, M. Erkintalo, S. G. Murdoch, and S. Coen, Opt. Lett. **39**, 5503 (2014).
[31] K. Luo, Y. Xu, M. Erkintalo, and S. G. Murdoch, Opt. Lett. **40**, 427 (2015).
[32] P. Parra-Rivas, E. Knobloch, D. Gomila, and L. Gelens, Phys. Rev. A **93**, 063839 (2016).
[33] P. Parra-Rivas, D. Gomila, and L. Gelens, Phys. Rev. A **95**, 053863 (2017).

[34] P. Parra-Rivas, D. Gomila, L. Gelens, and E. Knobloch, Phys. Rev. E **98**, 042212 (2018).
[35] M. Haelterman, S. Trillo, and S. Wabnitz, Opt. Lett. **17**, 745 (1992).
[36] S. Coen and M. Haelterman, Phys. Rev. Lett. **79**, 4139 (1997).
[37] M. Conforti, A. Mussot, A. Kudlinski, and S. Trillo, Opt. Lett. **39**, 4200 (2014).
[38] M. Conforti, F. Copie, A. Mussot, A. Kudlinski, and S. Trillo, Opt. Lett. **41**, 5027 (2016).
[39] F. Copie, M. Conforti, A. Kudlinski, A. Mussot, and S. Trillo, Phys. Rev. Lett. **116**, 143901 (2016).
[40] F. Bessin, F. Copie, M. Conforti, A. Kudlinski, A. Mussot, and S. Trillo, Phys. Rev. X **9**, 041030 (2019).